A New Model for Electric Force Microscopy and Its
Application to Electrostatically Generated Phase
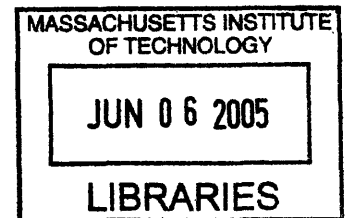Difference in Tapping Mode AFM

by

Peter Stone

Submitted to the Department of Materials Science
and Engineering in Partial Fulfillment of the
Requirements for the Degree of

Bachelor of Science

at the
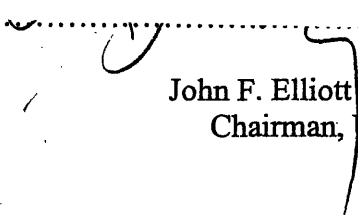
Massachusetts Institute of Technology

June 2005

The author hereby grants to MIT permission to reproduce and to distribute
publicly paper and electronic copies of this thesis document in whole or in part.

Signature of Author...
Department of Materials Science and Engineering
May 13, 2005

Certified by...
Francesco Stellacci
Finmeccanica Assistant Professor of Materials Science and Engineering
Thesis Supervisor

Accepted by...
Donald R. Sadoway
John F. Elliott Professor of Materials Chemistry
Chairman, Undergraduate Thesis Committee

A New Model for Electric Force Microscopy and Its
Application to Electrostatically Generated Phase Difference
in Tapping Mode AFM

by

Peter R. Stone

Submitted to the Department of Materials Science and
Engineering on May 13, 2005 in Partial Fulfillment of the
Requirements for the Degree of Bachelor of Science in
Materials Science and Engineering
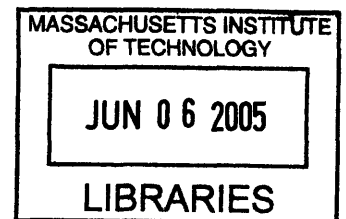
ABSTRACT

The harmonic force balance method was used to model and simulate electric force microscopy (EFM) and electrostatically generated phase difference in tapping mode AFM (EPTA) measurements. Simulations show that the harmonic force balance approach matches and explains EFM and EPTA experimental results well. Simulations also show that the model depended on both geometric and materials parameters.

The harmonic force balance model was subsequently used to directly simulate a previously performed EPTA experiment. Data obtained from the model showed a remarkable similarity to the experimentally obtained data, thus validating the use of the harmonic force balance model to simulate EPTA data.

Thesis Supervisor: Francesco Stellacci

Title: Finmeccanica Assistant Professor of Materials Science and Engineering

Table of Contents

Table of Figures

1. Introduction

Since its advent, the Atomic Force Microscope (AFM)[1] has proved a very powerful tool

for nanometer-scale characterization and modification of surfaces in air and liquid environments.

Its versatility is made evident by the broad spectrum of samples that can be imaged using AFM;

from high resolution images of biologically relevant materials, such as proteins[2], blood cells[3],

nucleic acids[4], and polymers[5], to atomic-resolution images of inorganic surfaces[6].

The ability of AFM to image such a variety of structures and interactions results from the

many modes of AFM operation that have been developed. The modes of AFM operation can be

defined at a number of levels. At the first level are the dynamics of the AFM tip and cantilever.

At this level we define the mode based on the electrical signal provided to the dither piezo that

controls cantilever displacement. This signal can be either direct current (DC) or alternating

current (AC). A DC signal leads to what is known as a static mode in which there is no external

oscillation of the cantilever probe tip. In contrast, an AC signal leads to the dynamic mode

where the tip is driven to oscillate.

At the next level we can define the mode of operation based on the *physical* relationship

between the tip and sample. The only DC mode of operation occurs if the tip and sample are

always kept in contact, an operation referred to as contact mode[7]. To ensure perpetual contact

between the tip and sample surface, the deflection of the cantilever is used in a feedback loop

and compared to a set point value which is assigned when there is no force between the sample

and tip. In contrast, there are two modes of AC operation differentiated by whether the

oscillating cantilever ever makes contact with the sample. If contact does occur at some point

during the cantilever's orbit, the cantilever is said to "tap" on the sample and we call it the

tapping mode[8]. If the cantilever never comes into contact then we have non-contact mode. In

the dynamic modes the feedback loop is maintained through a set point amplitude of the driving

oscillation of the dither piezo instead of the cantilever displacement.

In addition to the driving signal and experimental geometry, it is further possible to

define the mode based upon the dominant force between the tip and sample. If no additional

dominant forces exist in the experimental setup (e.g. electrostatic, magnetic, chemical, etc.) then

there are two principle modes of operation. If the driving force on the sample is normal to the

sample surface, it is referred to as Normal Force Microscopy. In contrast, when there is a lateral

driving force, it is Frictional (or Lateral) Force Microscopy. Furthermore, it is possible to alter

the system by adding a chemically functionalized probe tip (Chemical Force Microscopy)[9],

attaching specialized molecules to the end of the cantilever tip (e.g. carbon nanotubes)[10],

applying a voltage from the metallic probe tip to metallic substrate (Electric Force

Microscopy)[11], and other similar variations.

A newly developed offshoot of Electric Force Microscopy (EFM) is Electrostatically

generated Phase difference in Tapping mode AFM (EPTA).[12] The primary difference between

EFM and EPTA is that EFM is noncontact, while EPTA is, as its name implies, sometimes in

contact with the sample. Both EFM and EPTA work by measuring the phase delay between the

driving piezoelectric crystal oscillations and the tip oscillations. Thus, phase images are maps of

dissipative forces that take place at the tip-sample interface. Upon application of a tip-sample

bias, an increase in (the absolute value of) the phase response of a given material is observed.

This is due to the generation of new dissipative pathways due to the oscillating electric field (DC

voltage in a dynamic mode). The magnitude of the phase response is governed by the polarity of

the material; nonpolar regions show significantly less additional phase shift than polar or charged

regions. Furthermore, since EPTA is the difference between two phase images, other factors that

produce phase contrast are cancelled out, thus providing a high resolution map of electrostatic

dissipative forces which in turn can be viewed as a map of charge and polar domains of a given

sample (e.g. protein domains, etc.).

When approaching a model to simulate EFM and EPTA, several factors should be

considered. As mentioned above, there is a plethora of modes of AFM imaging available. With

such a variety of imaging modes already established in scientific method and more emerging

each year, any model of EFM should be robust and adaptable. However, such a model has

historically been difficult to find. This difficulty results primarily from the complex interactions

between tip and sample. Consequently, models tend to be quite complex, centered on

numerically solving nonlinear differential equations[13]. While such models were successful in

reproducing experimental results, Sebastian et al. identified two limitations of such methods

which deserve mention.[14] Firstly, numerical methods preclude identification of system

parameters in a straightforward manner. Secondly, and more importantly, the numerical

methods tend to be specific to only one AFM mode of operation. To overcome these

shortcomings, the model and methods developed in this paper expand upon the work of

Sebastian et al. who developed a very general model for simulating AFM results using a

harmonic force balance archetype. Sebastian et al. demonstrated the usefulness and accuracy of

such a method for the dynamic modes of AFM in both the tapping and noncontact regimes. The

harmonic force balance model is mathematically constructed such that tip-sample forces are pair

wise additive. Thus, we can expand the general form of the harmonic force balance by simply

adding in a tip to sample capacitive force.

The purpose of this paper is twofold. First, it is shown that the harmonic force balance

approach can indeed be expanded to simulate and model AFM modes which involve application

of a tip-sample bias by adding in a capacitive force term. Then, this approach is used to model

EPTA measurements on both polar and nonpolar materials to confirm the validity of the model

for EPTA.

2. Theory

2.1 The Harmonic Force Balance Equations

The following model for dynamic AFM in the conducting mode is adapted from

Reference 14. The following includes a summary of the main concepts from that model; a

complete derivation of the model can be found in that paper. In a dynamic mode, the cantilever

is driven to oscillate at or near its resonant frequency (ω_o) by a piezoelectric. In addition to this

driving force, modeled by the function g, the cantilever feels a dissipative force from its own

bending and air dampening.   Assume a linear time-invariant model G that models the cantilever

behavior. The model G takes as an input the drive force and the sample and outputs the

cantilever tip displacement and velocity, modeled by the function p. Also assume a function h

which maps the tip-sample separation and velocity back to the force on the cantilever due to the

sample. Thus we are viewing the system as an interconnection of two systems: the system G

which models the cantilever and h which models the sample.

It has been shown elsewhere[15,16] that the tapping-mode dynamics require the function p to

be periodic and have the same period as the driving force g. Since G is a linear time-invariant

operator and h, p, and g are periodic with the same period, it follows from the properties of linear

time-invariant operators and Fourier series that

$$h_k = g_k - \frac{p_k}{G(jk\omega)}. \tag{1}$$

All of the values on the right hand side of Equation (1) can be measured experimentally and, thus, provide us with a method for evaluating the Fourier coefficients for our tip-sample interaction force. Equation (1) can be simplified by choosing the forcing frequency of the dither piezo (ω) to be equal to or nearly equal to the resonant frequency of the cantilever. In this case, $G(jk\omega)$ tends to zero for all k > 1.[17] Thus we need only worry about the zeroth and first order Fourier coefficients of h, and we can write the function $p(t)$ as

$$p(t) = a\cos(\omega t + \phi) + p_o \qquad (2)$$

where a is the amplitude of the cantilever oscillation, ϕ is the phase difference and p_o is the DC offset.

2.2 Cantilever Model

By choosing an appropriate model and parameters for our cantilever model G, we can turn Equation (1) into a tractable optimization problem. It is already well established that a 2nd-order damped harmonic oscillator models an AFM cantilever well. Figure 1 shows a schematic of such a system where k is the spring constant of the cantilever and c is the dashpot coefficient. Mathematically we can write this system as

$$\ddot{p} + 2\xi\omega_o \dot{p} + \omega_o^2 p + h(p, \dot{p}) = g(t) \qquad (3)$$

where $\omega_o = \sqrt{k/m}$, $2\xi\omega_o = c/m$ and h is the force on the cantilever due to the sample normalized per unit mass. Combining equation (3) with the harmonic balance equation (1) we can write out the following relationship between Fourier coefficients

$$h_o - g_o + \omega_o^2 p_o = 0 \qquad (4)$$

$$h_{1r}(a, p_o, \phi) - g_{1r} + \Omega \frac{a}{2}\cos(\phi) - 2\xi\omega\omega_o \frac{a}{2}\sin(\phi) = 0 \tag{5}$$

$$h_{1i}(a, p_o, \phi) - g_{1i} + \Omega \frac{a}{2}\sin(\phi) + 2\xi\omega\omega_o \frac{a}{2}\cos(\phi) = 0 \tag{6}$$

where $\Omega = \omega_o^2 - \omega^2$.
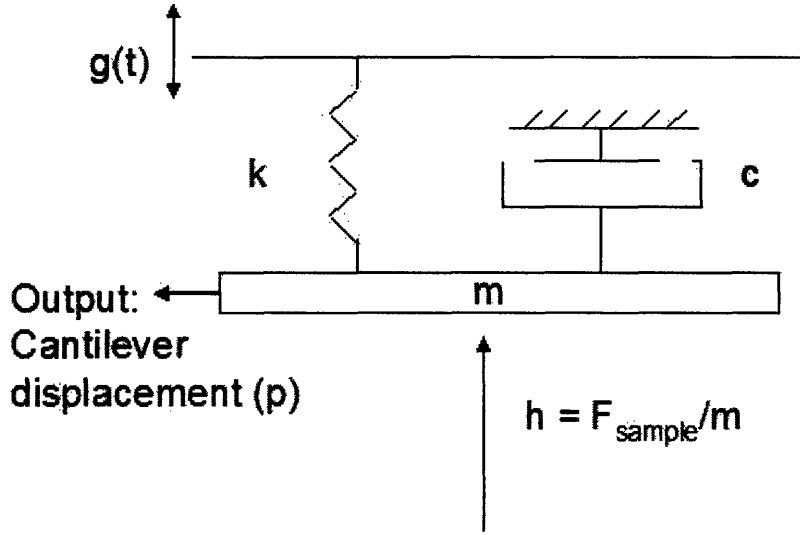
Figure 1: Damped harmonic oscillator model of an AFM probe tip (mass m) driven periodically by a dither piezo (g(t)) and subject to a force from the sample (h).

2.3 Tip-Sample Interaction Model

In order to make use of Equations (4) through (6), it is necessary to formulate a model

that will enable direct evaluation of the Fourier coefficients h_o, h_{1r} and h_{1i}. In other words, we

must expand our view of Figure 1 to include an explicit and analytical model for h. Recall that h

is a function of the tip-sample force. Thus, we can base our model off of high resolution force

spectroscopy data for a typical AFM tip-sample interaction. A schematic of such a curve is

shown in Figure 2. It should be noted that Figure 2 is accurate in the *absence* of an applied tip-

sample voltage. The electrostatic force will be added once the basic model is developed. At

long distances, i.e. beyond the length scale of dispersion, hydrophobic, hydrogen bonding, or

polar interactions, etc., there is no interaction force between the tip and the sample. As the tip is

brought closer to the sample it will begin to feel the attractive forces (the exact type of which is

dependent on the chemistry of the sample and possible functionalization of the tip). We will call

the distance from the sample surface at which these attractive forces begin to influence the

cantilever motion d. Further motion of the tip towards the sample will increase the attractive

forces until the tip is very close to the sample surface. At this point repulsive forces, both Born

repulsion between electron clouds of tip and surface and eventually the direct physical barrier of

the surface itself, begin to take over. However, since the length scale for Born repulsion

(typically $F_{born}(r) \propto r^{-12}$) is much less than that for the attractive forces, we can approximate the

repulsive forces as beginning at exactly the sample surface. Thus, we can define three regimes

of the tip sample interaction. If $l = 0$ defines the surface of our sample then for $l \leq 0$ the

interaction is repulsive, for $0 < l \leq d$ the interaction is attractive, and for $l > d$ there is no tip-
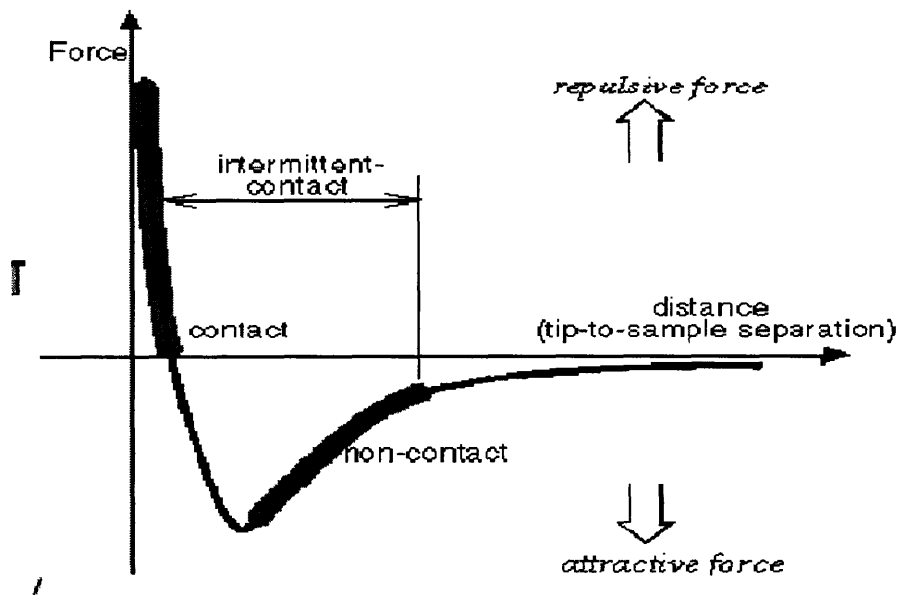
sample interaction.

Figure 2: Typical Force vs. Distance Interaction Between AFM Probe Tip and Sample[18]

A series of spring-damper systems models for the aforementioned physical dynamics well. Consider the left side of the schematic in Figure 3, where l represents the separation distance between the cantilever tip and sample. When $l > d$ the tip encounters no springs or dampers representing the no-interaction region. When the tip gets within a distance d of the sample surface, it encounters the spring-damper system that models the attractive interaction. The attractive force is represented by a spring with a negative spring constant $(-k = -m\omega_a^2)$ and any energy dissipation in this region is modeled by the damper, c_a. Similarly, once the repulsive regime is reached, the tip encounters a positive spring $(k = m\omega_b^2)$ and another damper, c_b. However, recall that this model is for dynamic modes of AFM. Therefore, the tip is not moving straight down to the sample, but is oscillating sinusoidally as it approaches the surface. Since, in general, the amplitude of oscillation of the tip (order of tens of nanometers) is greater than the length scale of the attractive or repulsive regions (order of single nanometers), the tip does not spend a complete orbit in any one region. Thus, the total force exerted by the surface on the tip will be a normalized superposition of the contributions from all relevant regions. Such normalization involves a straightforward calculation of the ratio of the amount of time the tip spends in a particular region during one cantilever orbit to the total time of the complete orbit (see below).
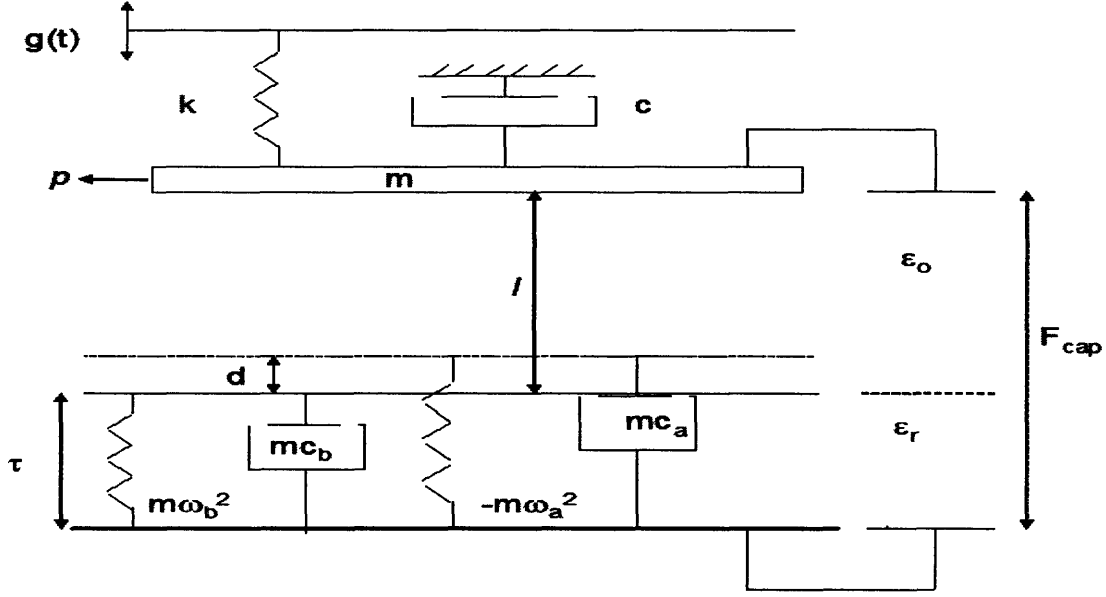
Figure 3: The piecewise linear cantilever-sample force interaction. It is composed of a spring-damper system representing repulsive forces when the tip comes into contact with the sample (subscripts b), a spring-damper system representing attractive forces between tip and sample (subscripts a), and a capacitor from the tip to the sample substrate. The capacitor contains two dielectrics- air and the sample. Springs account for attractive/repulsive forces and dampers for energy dissipation.

Now that the basic model for dynamic mode AFM has been established, it is possible to add in the contribution of applying a tip-sample voltage. This situation can be modeled as creating a capacitive force between the cantilever tip and the sample. In the general case, the capacitive force in the direction normal to the plane of the substrate can be written as

$$F_z(z) = -\frac{\partial C}{\partial z}\frac{V^2}{2} \tag{7}$$

where V is the voltage applied from tip to sample and the z-unit vector points from the tip to the surface. However, recall that our model requires a force per unit mass. Since $m = k / \omega_o^2$ we can write the capacitive component of h as

$$h_{cap} = \frac{F_z(z)}{m} = -\frac{\omega_o^2}{k}\frac{\partial C}{\partial z}\frac{V^2}{2}. \tag{8}$$

Now we can write the complete form of h for dynamic modes of AFM in the conducting mode as the sum of the contributions of the attractive, repulsive and capacitive forces per unit mass

$$h(p, \dot{p}) = -\frac{\omega_o^2}{k} \frac{\partial C}{\partial z} \frac{V^2}{2}, \; p \geq -l + d \tag{9}$$

$$h(p, \dot{p}) = -\omega_a^2(p + l - d) + c_a \, \dot{p} - \frac{\omega_o^2}{k} \frac{\partial C}{\partial z} \frac{V^2}{2}, \; -l \leq p < -(l-d) \tag{10}$$

$$h(p, \dot{p}) = \omega_b^2(p + l) - \omega_a^2(p + l - d) + c_a \, \dot{p} + c_b \, \dot{p} - \frac{\omega_o^2}{k} \frac{\partial C}{\partial z} \frac{V^2}{2}, \; p < -l. \tag{11}$$

Using Equations (9) through (11) we can calculate the zeroth and first order Fourier coefficients of h in each of the three force regimes

$$h_0(a, p_o) = h_{o,cap}, \; \text{if } p_o\text{-}a \geq -l + d$$

$$h_o(a, p_o) = \frac{a\omega_a^2}{\pi} \left(\sqrt{1 - s_1^2} - | s_1 | \, Cos^{-1}(| s_1 |) \right) + h_{o,cap}, \; \text{if } -l \leq p_o\text{-}a \leq l + d$$

$$h_o(a, p_o) = \frac{a\omega_a^2}{\pi} \left(\sqrt{1 - s_1^2} - | s_1 | \, Cos^{-1}(| s_1 |) \right) - \frac{a\omega_b^2}{\pi} \left(\sqrt{1 - s_s^2} - | s_s | \, Cos^{-1}(| s_s |) \right) + h_{o,cap},$$

if $p_o\text{-}a \leq l$ (12)

$$h_{1r}(a, po, \phi) = +h_{o,cap}, \; \text{if } p_o\text{-}a \geq -l + d$$

$$h_{1r}(a, p_o, \phi) = \frac{a \cdot Cos(\phi)}{2} \frac{\omega_a^2}{\pi} c_1 + \frac{a \cdot Sin(\phi)}{2} \frac{\omega \cdot c_a}{\pi} c_1 + h_{o,cap}, \; -l \leq p_o\text{-}a \leq l + d$$

$$h_{1r}(a, p_o, \phi) = \frac{a \cdot Cos(\phi)}{2} \frac{\omega_a^2}{\pi} c_1 + \frac{a \cdot Sin(\phi)}{2} \frac{\omega \cdot c_a}{\pi} c_1 - \frac{a \cdot Cos(\phi)}{2} \frac{\omega_b^2}{\pi} c_s + \frac{a \cdot Sin(\phi)}{2} \frac{\omega \cdot c_b}{\pi} c_2 + h_{o,cap},$$

if $p_o\text{-}a \leq l$ (13)

$$h_{1i}(a, p_o, \phi) = h_{o,cap}, \; \text{if } p_o\text{-}a \geq -l + d$$

$$h_{1i}(a, p_o, \phi) = \frac{a \cdot Sin(\phi)}{2} \frac{\omega_a^2}{\pi} c_1 - \frac{a \cdot Cos(\phi)}{2} \frac{\omega \cdot c_a}{\pi} c_1 + h_{o,cap}, \; -l \leq p_o\text{-}a \leq l + d$$

$$h_{1i}(a, p_o, \phi) = \frac{a \cdot Sin(\phi)}{2} \frac{\omega_a^2}{\pi} c_1 - \frac{a \cdot Cos(\phi)}{2} \frac{\omega \cdot c_a}{\pi} c_1 - \frac{a \cdot Sin(\phi)}{2} \frac{\omega_b^2}{\pi} c_2 - \frac{a \cdot Cos(\phi)}{2} \frac{\omega \cdot c_b}{\pi} c_2 + h_{o,cap},$$

if p_o-$a \le l$ (14)

where $c_1 = | s_1 | \sqrt{1 - s_1^2} - Cos^{-1}(| s_1 |)$, $c_2 = | s_2 | \sqrt{1 - s_2^2} - Cos^{-1}(| s_2 |)$, $s_1 = (-l + d - p_o)/a$, and

$s_2 = (-l - p_o)/a$. The terms *s1, c1, s2, and c2* are the previously mentioned normalization

factors that scale the Fourier coefficients according to the amount of time per cantilever orbit the

tip spends in each interaction regime.

Once $h_{o,cap}$ is evaluated (see Section 2.4) we can combine Equations (4) through (6) with

Equations (12) through (14) and obtain three equations in three unknowns, allowing us to

analytically calculate the amplitude, offset and phase of an AFM measurement. The

spring/damper parameters for the attractive and repulsive forces can be deduced from AFM

results taken with a tip-sample voltage of zero. Inserting these values into the harmonic balance

equations allows for simulation of dynamic AFM in the conducting mode as long as the

mechanical parameters of your cantilever tip (spring constant, etc.) and dielectric properties of

the sample are known.

2.4 Capacitance Models

The capacitor represented schematically in Figure 3 consists of the AFM probe tip and

the sample substrate. The capacitance of tip-substrate capacitor will, in general, be a function of

the distance between the tip and substrate and the dielectric constant of the material between the

tip and substrate. Let the distance between the probe tip and the substrate be represented by z.

Since the tip is oscillating, z is oscillating with the same frequency as the tip. Thus z will be a

function of the cantilever orbit ($p(t)$), the tip-sample separation (l), and the monolayer thickness (τ):

$$z(p,l,\tau) = p(t) + l + \tau . \tag{15}$$

Combining Equation (15) with the steady-state periodic solution for the cantilever orbit given in Equation (2), we obtain the following time-dependent relationship for the distance between the tip and the substrate

$$z(t) = a \cdot Cos(\omega t + \phi) + p_o + l + \tau \tag{16}$$

Between the two plates of the tip-sample capacitor is a monolayer, which acts as a dielectric. To calculate the capacitance of the tip-sample capacitor it is, therefore, useful to define an effective permittivity, ε', that is a function of the dielectric constant of the monolayer, and the ratio of monolayer thickness to total tip-substrate separation. Recall that a capacitor that contains two dielectrics can be modeled as two capacitors in series. To a rough approximation (see Section 3.1) this system can be modeled by the parallel plate approximation. Under this approximation we can write that the effective permittivity of the tip-substrate capacitor is

$$\varepsilon' = \frac{\omega}{2\pi} \int_{0}^{\frac{2\pi}{\omega}} \frac{(a \cdot Cos(\omega t + \phi) + p_o + l + \tau) \cdot \varepsilon_o \cdot K}{\tau + K(a \cdot Cos(\omega t + \phi) + p_o + l)} dt \tag{17}$$

where ε_o is the permittivity of free space, ε_r is the permittivity of the monolayer, and the dielectric constant, K, of the monolayer is $\varepsilon_r/\varepsilon_o$. Equation (17) is, in effect, an average of the dielectric properties of the two dielectrics, air and monolayer, weighted by the orbit of the cantilever. To utilize Equation (17), the harmonic force balance equations should be solved in the absence of the capacitive force. This will give a rough estimate of the cantilever orbit through the values a and p_o. Unlike the phase, these values show little change when a voltage is applied. These values should be used in Equation (17) along with the known parameters for tip-

sample separation (l), monolayer thickness, τ, and monolayer dielectric constant, K. Equation (17) must be evaluated for each experiment to obtain an accurate estimate for the effective permittivity because it is a very sensitive function of the orbit of the cantilever since it decays with the reciprocal of capacitor thickness. Note that when $z(t) = \tau$ the effective permittivity simplifies to $K\varepsilon_0$, and when $z(t)$ is very large the effective permittivity tends to ε_0. Both of these make sense physically as they correspond to the cases where the capacitor contains only the monolayer as a dielectric and where the monolayer thickness is negligible respectively. For a full derivation of Equation (17) please see Appendix A.

2.4.1 Parallel Plate Capacitor Model

The parallel plate capacitor model requires us to project the three dimensional AFM probe tip into a two dimensional geometry. Therefore, the main assumption of the parallel plate capacitor model is that an AFM probe tip of radius, R, can be modeled as a plate of area, A = πR^2. Neglecting fringe effects, this plate only interacts with its projection onto the relatively flat sample surface of equal area. Recall from introductory physics the capacitance of this geometry

$$C_{p.p.} = \frac{\varepsilon' \cdot A}{z}.$$ (18)

Combining Equations (18), (16), and (7) gives us the capacitive force per unit mass of the parallel plate model

$$h_{p.p.} = \frac{\omega^2 \varepsilon \pi R^2 V^2}{2k(a \cdot Cos(\omega t + \phi) + l + p_o + \tau)^2}$$ (19)

which has zeroth and first order Fourier coefficients given by

$$h_o = \frac{l + p_o + \tau}{\left(-a^2 + (l + p_o + \tau)^2\right)^{3/2}} \cdot \frac{\omega^2 \varepsilon \pi R^2 V^2}{2k}$$ (20)

$$h_{1r} = \frac{2a}{\left(-a^2 + (l + p_o + \tau)^2\right)^{3/2}} \cdot \frac{\omega^2 \varepsilon \pi R^2 V^2}{2k} \cdot Cos(\phi) \tag{21}$$

$$h_{1i} = \frac{2a}{\left(-a^2 + (l + p_o + \tau)^2\right)^{3/2}} \cdot \frac{\omega^2 \varepsilon \pi R^2 V^2}{2k} \cdot Sin(\phi). \tag{22}$$

The detailed derivation of Equations (20) through (22) is given in Appendix B.

2.4.2 Sphere-Plane Capacitor Model

A better approximation of the tip-sample interactions models the tip as a sphere of radius R interacting with a semi-infinite plane. The sphere-plane geometry is widely used to model dispersion, dipole, van de Waals, and other interactions[19] between AFM probe tips and samples and is thusly pursued as an electrostatic model. While calculation of these interparticle and intersurface forces is relatively straightforward, the electrostatic case is more complicated. The explicit solution for sphere-plane capacitive force is known:[20]

$$F = 2\pi \varepsilon V^2 \sum_{n=1}^{\infty} \left[Csch(n\alpha)(Coth(\alpha) - n \cdot Coth(n\alpha))\right]. \tag{23}$$

However when the time dependent tip-substrate distance is substituted into the infinite sum, it becomes unwieldy to calculate an analytical solution over the number of terms it takes for the series to converge. Oyama et al.[21] simplified the above general solution to a rational series for a Scanning Tunneling Microscope (STM) probe tip

$$F = \sum_{i=0}^{n} \frac{2\sqrt{s^2 - 1}}{\left(s + \sqrt{s^2 - 1}\right)^{i+1} - \left(s - \sqrt{s^2 - 1}\right)^{i+1}} \tag{24}$$

where $s = z/R + 1$. This series converges rather quickly (in less than ten terms) for tip-sample separations much greater than the probe tip radius, but takes thousands of terms to converge at length scales equal to or less than the probe tip radius. Hudlet et al.[22] simplified the equations for

this geometry through a few mathematical tricks and approximations. Their result for the capacitive force between surface and plane is given by

$$F_z(z) = \pi\varepsilon'\left(\frac{R^2}{z(z+R)}\right)V^2 \tag{25}$$

It should be noted that Equation (25) is an approximation with finite error. It reaches a maximum error of around 3% when the ratio of sphere-plane separation to sphere radius is around 1/3. However, for most sphere-plane separations the error is < 1 % and provides an accurate model. Thus Equation (25) provides an accurate, yet manageable capacitive force expression that can be used in the harmonic force balance equations

$$h_{s-p} = \frac{\omega^2 \pi\varepsilon' V^2}{k} \cdot \frac{R^2}{\left(a \cdot Cos(\omega t + \phi) + p_o + l + \tau\right) \cdot \left(a \cdot Cos(\omega t + \phi) + p_o + l + \tau + R\right)} \tag{26}$$

which can be written as a Fourier series with coefficients

$$h_o = \frac{\pi\varepsilon' R^2 V^2 \omega^2}{k} \cdot \frac{\dfrac{1}{\sqrt{-a^2 + (l + p_o + \tau)^2}} - \dfrac{1}{\sqrt{-a^2 + (l + p_o + \tau + R)^2}}}{2 \cdot R} \tag{27}$$

$$h_{1r} = \frac{\pi\varepsilon' R^2 V^2 \omega^2 Cos(\phi)}{k \cdot a \cdot r}\left(\begin{array}{l} -\dfrac{l}{-a^2 + (l + p_o + \tau)^2} - \dfrac{p_o}{-a^2 + (l + p_o + \tau)^2} - \dfrac{\tau}{-a^2 + (l + p_o + \tau)^2} + \\[4mm] \dfrac{l}{-a^2 + (l + p_o + \tau + R)^2} + \dfrac{p_o}{-a^2 + (l + p_o + \tau + R)^2} + \\[4mm] \dfrac{R}{-a^2 + (l + p_o + \tau + R)^2} + \dfrac{\tau}{-a^2 + (l + p_o + \tau + R)^2} + \end{array}\right) \tag{28}$$

$$h_{1i} = \frac{\pi\varepsilon' R^2 V^2 \omega^2 Sin(\phi)}{k \cdot a \cdot r}\left(\begin{array}{l} -\dfrac{l}{-a^2 + (l + p_o + \tau)^2} - \dfrac{p_o}{-a^2 + (l + p_o + \tau)^2} - \dfrac{\tau}{-a^2 + (l + p_o + \tau)^2} + \\[4mm] \dfrac{l}{-a^2 + (l + p_o + \tau + R)^2} + \dfrac{p_o}{-a^2 + (l + p_o + \tau + R)^2} + \\[4mm] \dfrac{R}{-a^2 + (l + p_o + \tau + R)^2} + \dfrac{\tau}{-a^2 + (l + p_o + \tau + R)^2} + \end{array}\right) \tag{29}$$

3. Results and Discussion

3.1 Parallel Plate versus Sphere-Plane

Figure 4 is a comparison of simulation data obtained from both the parallel plate and sphere-plane capacitive models with a tip radius of 25 nm in the non-contact regime. The simulation parameters used were $\omega_a = 0.31$, $\omega_b = 3.03$, $c_a = 0 \ \mu s^{-1}$, $c_b = 1.45 \ \mu s^{-1}$, $k = 4$ N/m, $\xi = 0.0038$, $\omega = \omega_o = 2\pi*73,881$ Hz, $\varepsilon' = 1.2\varepsilon_o$, $d = 1.695$ nm, and $\tau = 8$ nm. Data from the parallel plate capacitor model tended to exceed the corresponding values from the sphere plane model by at least a factor of two. The discrepancy was more pronounced at larger tip radii (not shown) and voltages. This can be attributed to the inherent assumption in the parallel plate model that the AFM tip is flat. The conical nature of the AFM tip means that not all points within a radii's distance of the center of the tip are at the same height above the sample. In fact, most of these points are farther away. This leads to an overestimation of the electric field strength upon application of the tip-sample bias, and, thus, also overestimates the tip-sample dissipative forces. This leads to larger changes in phase than were expected from experimental data (see below), while the sphere-plane model predicted the magnitude of the phase shift much more accurately.

DeltaPhi (degrees)

-2.5 -2 -1.5 -1 0 0.5 1 1.5 2 2.5

-2

-4

-6

-8

-10

-12

-14

-16

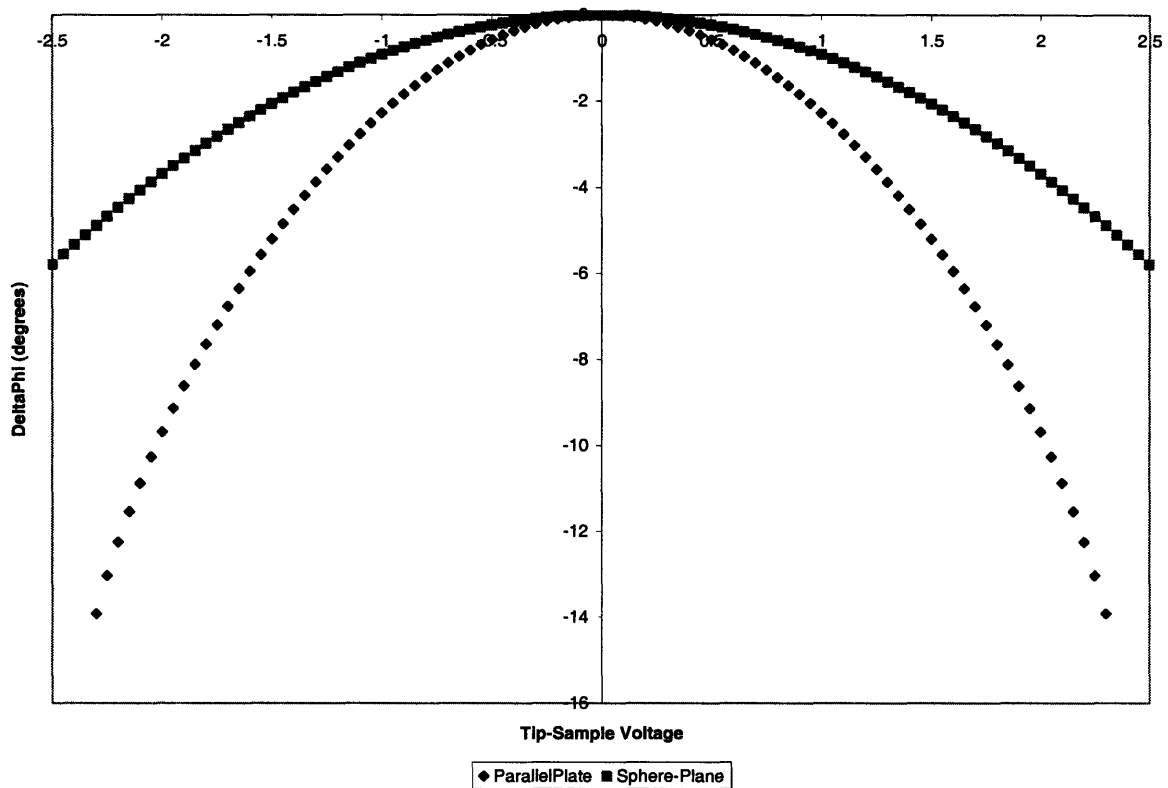**Tip-Sample Voltage**

◆ ParallelPlate   ■ Sphere-Plane

Figure 4: Comparison of data from the parallel plate and sphere-plane capacitive models. Note the large difference between the two models, especially at higher voltages. Also note that the x-axis only goes from -2.5V to 2.5V since the parallel plate model could not be solved at voltages on larger magnitude than these extremes.

Furthermore, the parallel plate model broke down at low voltages for all tip radii. For example, at a tip radius of 50 nm the harmonic force balance equations could not be solved when $V > 1.3$ volts using traditional root finding mechanisms (such as the secant or bisection methods in the *Mathematica* software). Since experimental data in EFM and EPTA are generally taken with tip-sample bias of up to 7-10 volts, this was clearly a problem. Thus, the parallel plate capacitor model, while it did accurately predict the expected quadratic shape of the delta phi versus voltage curves, was not pursued due to its large numerical inaccuracy and difficulty in solving the equations at intermediate tip-sample biases.

3.2 Sphere-Plane Capacitor Model

In order to demonstrate the validity of the harmonic force balance model the calculations of Sebastian et al. were reproduced, and then a tip-sample capacitive force was added to their equations. The simulation parameters are the same as noted in Section 3.1. Figure 5 compares these calculations over all regions of interaction. As expected, an increase in the absolute value of the phase occurs in all regions, corresponding to the electrostatic dissipative forces associated with the applied voltage. Furthermore, the capacitive force is clearly longer range than the intermolecular attractive and repulsive forces between the tip and sample since a deviation from the -90 degree baseline occurs at a larger tip-sample separation in the case where a voltage was applied. The longer range interaction is important because it demonstrates that the model can be used to simulate EFM in lift mode since a change in phase is observable in an entirely noncontact regime.

It should be noted that there is a loss of information at a tip-sample separation corresponding to the case where the tip oscillations barely bring it in contact with the monolayer ($a \sim l$). This is due to the piecewise-linear nature of the tip-sample interaction functions. Very near (~0.1 nm) to the transition from one set of equations to the other, it is difficult to tell which set of equations to use. However, since EFM and EPTA are performed at a constant value of l (tip-sample separation) this is not a large problem as long as l is chosen such that it is clearly within the appropriate regime, the noncontact region for EFM and the tapping mode region for EPTA.
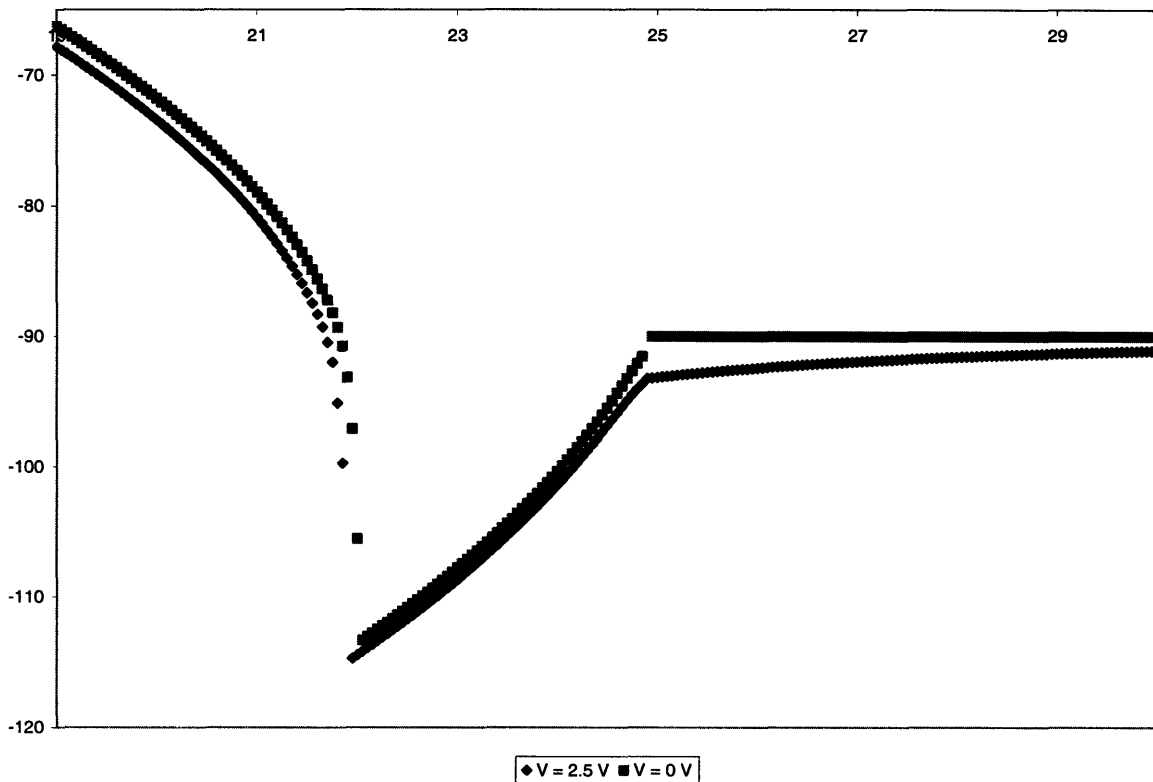
Figure 5: Effect of tip-sample bias on phase in all regions of interaction. Note that when the tip-sample separation is greater than 25 nm the tip sample bias leads to an observable change in phase. Since this is in the non-contact region, it demonstrates the viability of this model to simulate EFM experiments in the lift mode.

The effect of changing the simulation parameters was studied next. Figure 6 shows the effect of tip-radius size on the change in phase (delta phi)- i.e. the value of the phase in the conducting mode case minus the value of the phase in the non-conducting case. Thus, delta phi is proportional to the change in dissipative forces that occurs when a voltage is applied. The calculations used to obtain Figure 6 were evaluated in order to simulate electrostatic interactions in the tapping mode. From Figure 5 it is readily observable that the tip starts to make constant with the sample when the tip-sample separation is approximately 22 nm. This suggests that the oscillation amplitude of the probe tip under the electrostatic interactions is around 22 nm since repulsive forces only occur, to a first approximation, once the tip makes contact with the sample.

23

Thus, a tip sample separation of 20 nm was chosen for the calculations occurring from this point

forward. This value guarantees that we are in the tapping mode, as well as avoids the

mathematical complications of being near the transition between regimes. All other systems
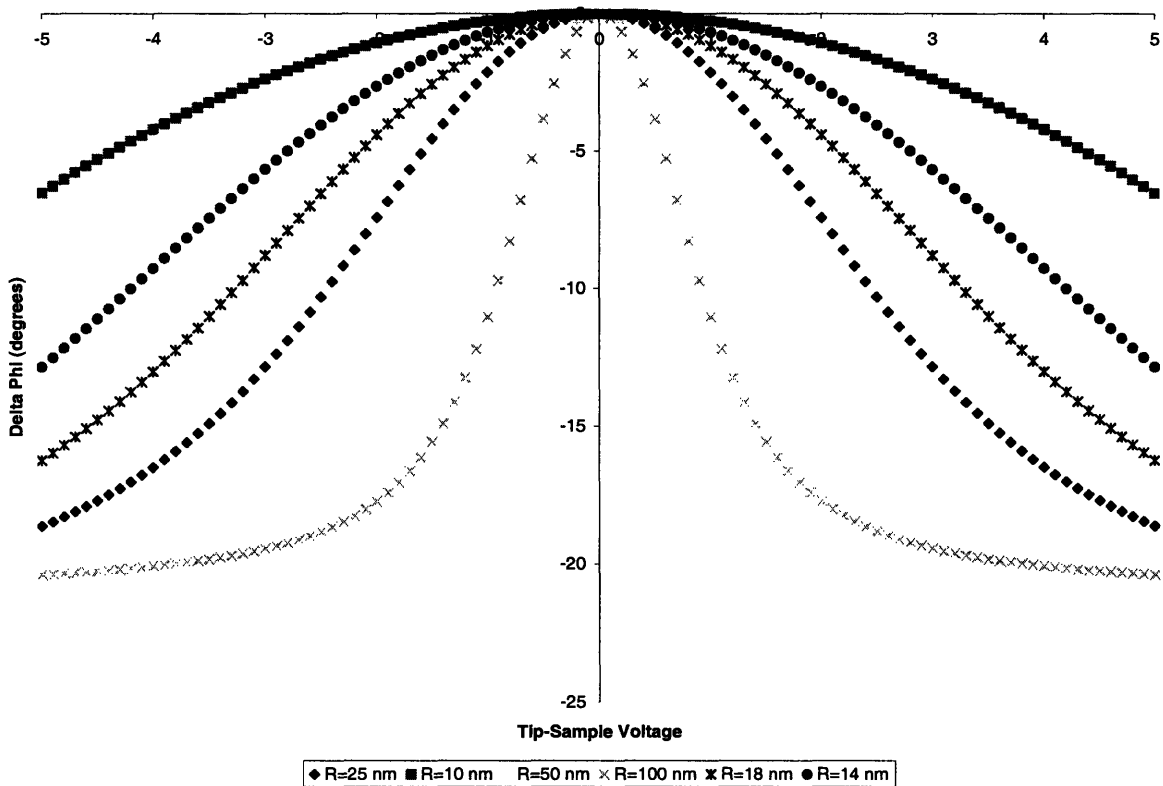
parameters were kept the same.

Figure 6: Effect of tip radius size on phase shift. Clearly an increase in radius leads to greater phase shift and electrostatic force dissipation, though it appears that a saturation point is reached at higher tip-sample voltages.

From Figure 6 it is easily seen that increasing the radius of the AFM probe tip increases

the phase shift at a given voltage. This makes sense because both the capacitance and the

capacitive force scale with the size of the probe tip. For small capacitive forces the delta phi

versus voltage functions take on a quadratic form. A quadratic fit for the R = 10 nm case in

Figure 6 has a correlation coefficient of 0.999. This value steadily decreases as the tip radius is

increased. Furthermore, the data suggest that there is some maximum phase shift that occurs at

high capacitive forces. Both of these trends are in agreement with observations made by an experimentalist performing EPTA on dielectric monolayers.[23]

Figure 7 shows the effect of changing the dielectric constant of the monolayer on the delta phi versus voltage data for a tip radius of 10 nm. Values of k = 40 N/m, ω_0 = 300 kHz and τ = 1.5 nm were used since these correspond to the properties of the cantilevers used in the EPTA experiments described in the Section 3.4. There is a clear increase in phase shift with the increase in dielectric constant. Figure 7 demonstrates the underlying principle of EPTA- polar and nonpolar entities can be differentiated by an AFM probe tip applying a voltage by their relative phase shifts. Larger phase shifts, corresponding to more electrostatic dissipative pathways, occur in polar materials, whereas phase shifts due to an applied voltage are barely observable in nonpolar materials where such pathways are less likely to form.

Tip-Sample Voltage

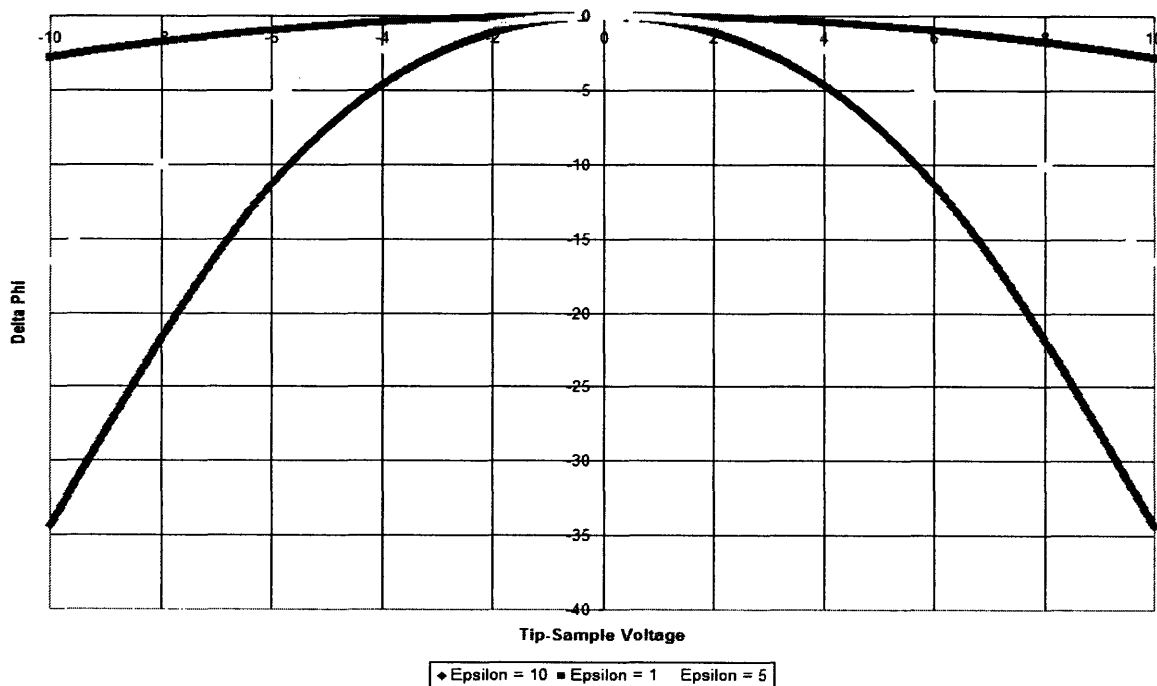◆ Epsilon = 10   ■ Epsilon = 1   Epsilon = 5

Figure 7: Effect of monolayer dielectric constant on phase shift. An increase in the dielectric constant, which corresponds to an increase in the polarity of the monolayer, leads to greater electrostatic dissipation and, hence, a larger phase shift. This figure demonstrates the validity of the underlying principle of EPTA: An

unfunctionalized AFM probe tip can differentiate between polar and nonpolar entities when a tip-sample bias is applied.

3.3 Simulation of an EPTA Experiment Using the Harmonic Force Balance Model

In light of the observations shown in Figure 7, the harmonic force balance model was used to reinforce and interpret the findings of an EPTA experiment. Two monolayers, one made of molecules terminated with a polar group (6-mercapto-1-hexanol, **MH**, $HS-(CH_2)_6-OH$), and the other made of nonpolar molecules (1-hexanethiol $HS-(CH_2)_5-CH_3$), were grown on a (111) Gold substrate (see Reference 12 for synthesis details). Both samples were imaged in the tapping mode under the influence of a tip-sample bias. While the application of a voltage did not affect the height images of either sample, the phase images are altered, as shown in Figure 8. The nonpolar monolayer shows no observable change in phase with application of the tip sample bias. However, there is a marked change in the phase of the polar monolayer upon application of bias. Such findings are in agreement with the general trends shown in Figure 7, though an exact quantitative relationship should not be made because the simulation parameters used in those calculations do not mirror the experimental conditions at which the data in Figure 8 were taken.
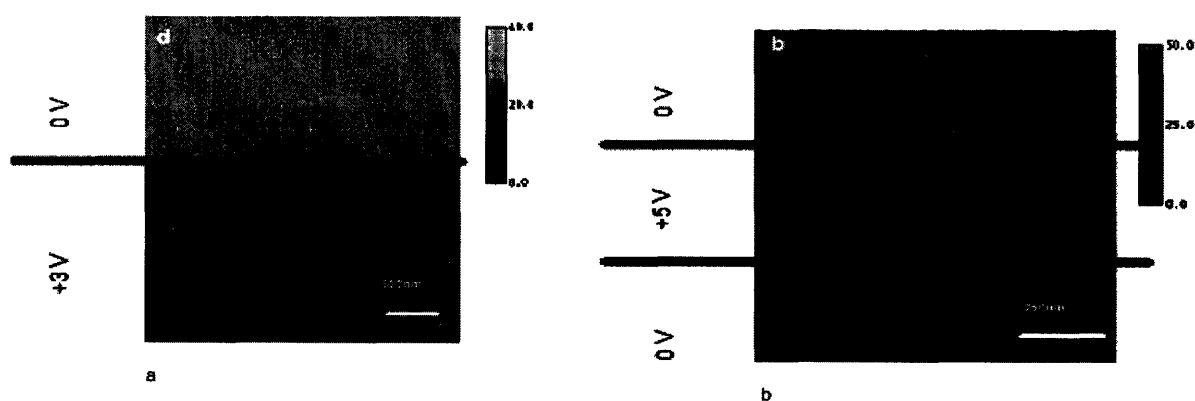

Figure 8: AFM images of a) Mercapto Hexanol (polar) and b) Hexane Thiol (nonpolar) monolayers with and without an applied tip-sample bias. A clear phase shift is observed in the polar monolayer when a bias is applied, but no such change can be seen in the nonpolar monolayer.[14]

A more quantitative analysis of the polar monolayer was undertaken next. Figure 9

shows the observed experimental phase shift of the polar monolayer at selected tip sample

voltages. A best-fit trend line is added to emphasize the quadratic nature of the results. It should

be noted that this plot is of the absolute magnitude of the phase shift. The only effect of this

convention is that the data are reflected in the y-axis. Nonetheless, the phase shift still represents

an increase in dissipative forces between tip and sample. The simple quadratic nature of the

experimental data is clearly in agreement with the plots in Figures 5 through 7 which show
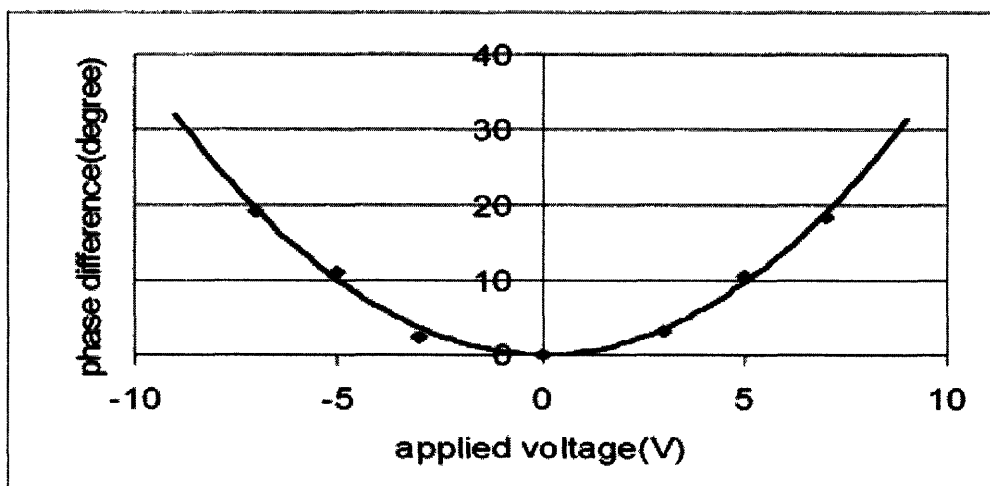
similar behavior at low capacitive forces.

Figure 9: Effect of applied voltage on phase difference in the Mercapto Hexanol monolayer.[12]

The simulation of the results in Figure 9 was run by virtual "growth" of the monolayers

on the setup of Sebastian et al. As mentioned above, since EPTA functions by looking at the

change in phase, other factors that cause phase contrast are cancelled out. Thus, we can utilize

the estimated tip-substrate attractive and repulsive parameters from Sebastian et al. to reproduce

the cantilever orbit. However, we do need to worry about the parameters that affect the tip-

sample capacitive force: ω_0, k, K, R, and τ.

For the parameters dependent on the cantilever properties (ω_o, k, and R), the nominal manufacturers' values were used. While there can be as much as a factor of 4 variance in these properties from probe tip to probe tip, using the median values for these parameters provides a rough estimation of the cantilever behavior. For the probe tip of interest, a Veeco NanoprobeTM tip (Model #: RTESP), these values are $\omega_o = 300$ kHz, $k = 35$ N/m, and R = 10 nm. Furthermore, we know that the monolayer thickness, τ, is on the order of 1.3 nm. The final parameter we need is the effective dielectric constant, ε', which is a function of the dielectric constant of the monolayer, K. Since the –SH functionalization of the monolayer serves to anchor it to the substrate, we can, to a first approximation, view the monolayer as being composed of tethered hexanol molecules which have a dielectric constant of roughly 14. Using the method detailed in Appendix A (V = 0 values for a and p_o were 20.39 nm and 0.179 nm respectively), ε' was evaluated to be $8.61\varepsilon_o$. With all the parameters accounted for, the harmonic force balance equations can be solved. The results of these calculations are shown in Figure 10 along with the data from Figure 9. Considering the approximations that were made to perform the calculation, the two data sets are in very good agreement especially at small voltages. Thus, a simple sphere-plane capacitor model can accurately reproduce the behavior of EPTA.
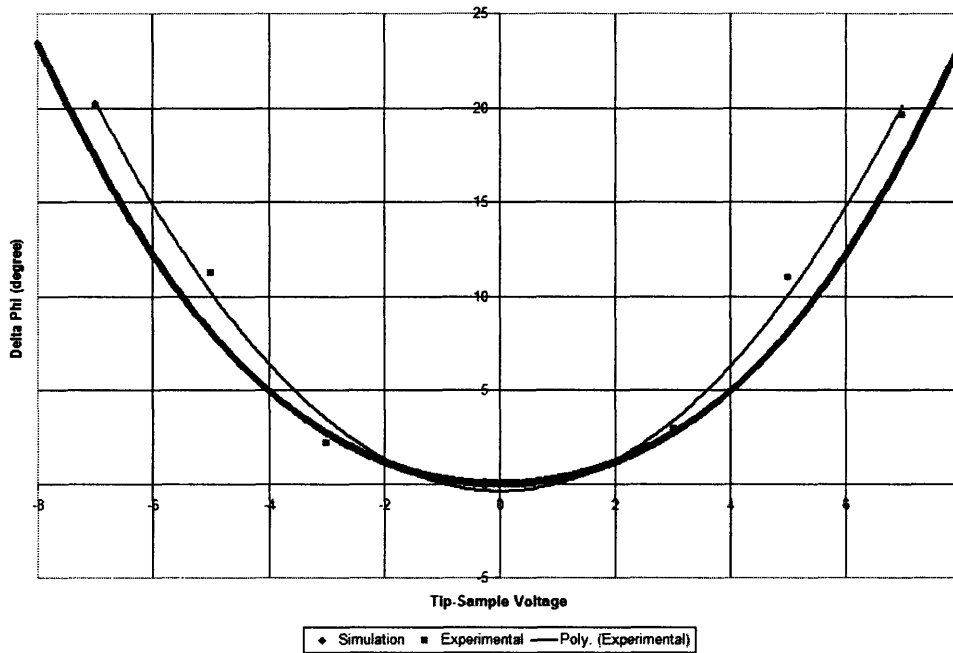
Figure 10: Comparison of simulation and experimental EPTA on Mercapto Hexanol monolayer. The simulation is in good agreement with the experimental data.

3.4 Limitations and Suggestions for Future Improvement

It should be noted, as in the original case of Sebastian et al., that because only the zeroth

and first order Fourier coefficients are used in the harmonic force balance equations, the tip-

sample interaction force is filtered by the cantilever when it is operating near its resonant

frequency. Thus, the finer features of the tip-sample interaction are lost in this model. If it

becomes possible to measure higher harmonics of the cantilever oscillations then this can be

easily incorporated by expanding the harmonic balance equations for k > 1.

Perhaps a larger limitation is the breakdown of the sphere-plane capacitor model at high

voltages. While the model is accurate at small capacitive forces, anomalous behavior is observed

at higher voltage for small tip radii. Figure 11 shows an expanded view of the radial dependence

of the delta phi versus voltage curves. While for larger probe tip radii there appears to be a

29

consistent saturation value for delta phi, a crossover occurs for smaller radii (R < 20 nm). The

origin of this behavior is unclear, but it may be due to the underlying assumptions made to derive

this model. This behavior is only a problem at voltages rarely used in EFM and EPTA

experiments and so does not present a large problem to the results heretofore presented.

However, determination of the origin of this behavior should be done in the future to better

understand the underlying principles of this model.
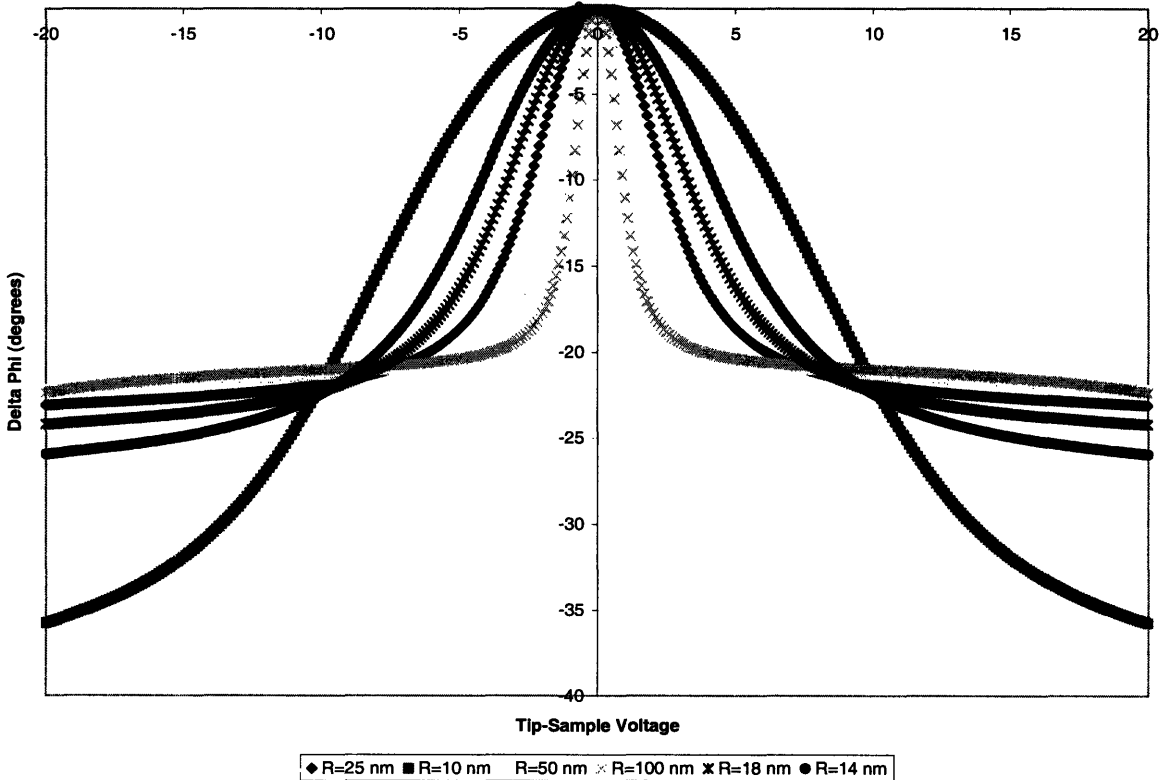
Figure 11: Expanded view of the radial dependence of phase shift versus tip-sample voltage. Note the anomalous behavior at V > 10 Volts.

Clearly, further refinement is needed to produce even more accurate results and expand

the number of possible applications for the harmonic force approach. The sphere-plane

geometry only takes into account the spherical contribution of the AFM tip ignoring the conical

part above it. This is, perhaps, why the model slightly underestimates the phase difference with

respect to experimental results (see Figure 10). A more accurate expression for the tip-sample

capacitive force that includes the conical contribution has been derived by others.[22] However, its

complex form made it undesirable for this simple model. Furthermore, an exact expression for

the effective dielectric constant would be desirable over the numerical approximation presented

in Appendix A. Such an expression would, perhaps, allow for an accurate determination of a

material's dielectric constant from EPTA results and, thus, further expand the function of the

harmonic force model.

4. Conclusions

It has been shown that the harmonic force balance perspective provides an effective

method by which to model and simulate both the EFM and EPTA modes of AFM. This

relatively simple model is desirable for a few of reasons. Firstly, since it is derived from the

harmonic force balance approach, it can easily be adapted to other, more complex, applications

by simply adding in another term to the tip-sample interaction function, h. This is particularly

important as atomic force microscopy experiments become integrated with other apparatuses.

Secondly, and more importantly, the model takes into account both geometric and materials

parameters to produce its results. It is a robust function of both the particular AFM setup and the

sample being investigated, thus making it superior to models which only take into account one of

these factors. These underlying factors make modeling of EPTA possible using this method.

5. Appendices

Appendix A: Effective Dielectric Constant Approximation

A capacitor that contains two dielectric media can be modeled as two capacitors in series. Recall that we can write an equivalent capacitance of two parallel plate capacitors in series as

$$\frac{1}{C_{eq}} = \frac{1}{C_1} + \frac{1}{C_2}$$ (A1)

where C_1 is the capacitance of the monolayer component of the two dielectric capacitor and C_2 is the capacitance of the air gap between the probe tip and sample. Solving for C_{eq} and expanding C_1 and C_2 we can write

$$C_{eq} = \frac{K \cdot \varepsilon_o \cdot A}{z(t) + (\varepsilon_r - 1) \cdot (z(t) - \tau)}.$$ (A2)

We can set the right side of Equation (A2) equal to the capacitance of an 'effective' capacitor to obtain the effective permittivity.

$$\frac{K \cdot \varepsilon_o \cdot A}{z(t) + (\varepsilon_r - 1) \cdot (z(t) - \tau)} = \frac{\varepsilon' \cdot A}{z(t)}$$ (A3)

where ε' is the equivalent permittivity of the entire tip-sample capacitor.. We can solve the above for ε' we obtain

$$\varepsilon' = \frac{\varepsilon_o K \cdot z(t)}{\tau + K \cdot (z(t) - \tau)}.$$ (A4)

Equation (A4) represents a weighted average of the permittivities of the two capacitor segments normalized by the path the cantilever takes. Note that when ε_o and ε_r are equal (i.e. there is no monolayer, only a tip and substrate) the effective permittivity is equal to ε_o. Substituting in an expression for z(t) we obtain

$$\varepsilon' = \frac{(a \cdot Cos(\omega t + \phi) + p_o + l + \tau) \cdot \varepsilon_o \cdot K}{\tau + K(a \cdot Cos(\omega t + \phi) + p_o + l)} \qquad (A5)$$

Equation (A5) gives the effective capacitance at any given time during an AFM experiment. To utilize it, the V=0 simulation must be run first and values obtained for a, p_o and ϕ. These values will provide a rough estimate of the orbit of the cantilever during the EFM experiment. To obtain the effective capacitance over the whole timescale, we can take the time-averaged integral of Equation (A5) and plug in the known values for tip-sample separation distance, monolayer thickness, and monolayer dielectric constant. Doing so, we can numerically estimate the effective capacitance of the tip-sample capacitor as

$$\varepsilon' = \frac{\omega}{2\pi} \int_{0}^{\frac{2\pi}{\omega}} \frac{(a \cdot Cos(\omega t + \phi) + p_o + l + \tau) \cdot \varepsilon_o \cdot K}{\tau + K(a \cdot Cos(\omega t + \phi) + p_o + l)} \, dt \qquad (A6)$$

33

Appendix B: Evaluation of Fourier Coefficients in the Parallel Plate Capacitor Model

Recall Equation (19) which details the capacitive force per unit mass between two parallel plate capacitors

$$h_{p.p.} = \frac{\omega^2 \varepsilon \pi R^2 V^2}{2k \left(a \cdot Cos(\omega t + \phi) + l + p_o + \tau\right)^2} . \tag{B1}$$

Now the Fourier coefficient of h_o can be found by

$$h_o = \frac{\omega}{2\pi} \int_{\frac{-\pi}{\omega}}^{\frac{\pi}{\omega}} h(t) \cdot dt \tag{B2}$$

since h has period $2\pi/\omega$. Thus we can write

$$h_o = \frac{\omega}{2\pi} \cdot \frac{\omega^2 \varepsilon \pi R^2 V^2}{2k} \int_{\frac{-\pi}{\omega}}^{\frac{\pi}{\omega}} \frac{1}{\left(a \cdot Cos(\omega t + \phi) + l + p_o + \tau\right)^2} dt \tag{B3}$$

We can eliminate the ϕ in Equation (B3) since we are integrating over one full period of the function and thus the phase lag of the function is inconsequential. Equation (B3) evaluates to Equation (20) in the Section 2.4.1.

The first order Fourier coefficients, h_{1r} and h_{1i} are evaluated as

$$h_{1r} = \frac{\omega}{\pi} \int_{\frac{-\pi}{\omega}}^{\frac{\pi}{\omega}} Cos(\omega t) \cdot h(t) \cdot dt \tag{B4}$$

$$h_{1i} = \frac{\omega}{\pi} \int_{\frac{-\pi}{\omega}}^{\frac{\pi}{\omega}} Sin(\omega t) \cdot h(t) \cdot dt . \tag{B5}$$

To simplify the evaluation of this integral, we can take advantage of the identities

$Cos(\omega t) = Cos(\omega t + \phi) \cdot Cos(\phi) + Sin(\omega t + \phi)Sin(\phi)$ and

$Sin(\omega t) = Sin(\omega t + \phi) \cdot Cos(\phi) - Cos(\omega t + \phi) \cdot Sin(\phi)$. We can write

$$h_{1r} = \frac{\omega}{\pi} \cdot \frac{\omega^2 \varepsilon \pi R^2 V^2}{2k} \cdot \int_{\frac{-\pi}{\omega}}^{\frac{\pi}{\omega}} \left(\frac{Cos(\phi)Cos(\omega t + \phi)}{(a \cdot Cos(\omega t + \phi) + l + p_o + \tau)^2} + \frac{Sin(\phi)Sin(\omega t + \phi)}{(a \cdot Cos(\omega t + \phi) + l + p_o + \tau)^2} \right) dt \quad \text{(B6)}$$

$$h_{1i} = \frac{\omega}{\pi} \cdot \frac{\omega^2 \varepsilon \pi R^2 V^2}{2k} \cdot \int_{\frac{-\pi}{\omega}}^{\frac{\pi}{\omega}} \left(\frac{Cos(\phi)Sin(\omega t + \phi)}{(a \cdot Cos(\omega t + \phi) + l + p_o + \tau)^2} - \frac{Sin(\phi)Cos(\omega t + \phi)}{(a \cdot Cos(\omega t + \phi) + l + p_o + \tau)^2} \right) dt \quad \text{(B7)}$$

The terms of Equations (B6) and (B7) with the $Sin(\omega t + \phi)$ terms in the numerator are even,

symmetric, periodic functions and, therefore, their integrals go to zero. Thus, we only need to

evaluate the $Cos(\omega t + \phi)$ terms in the numerator. Using the same trick as in the zeroth order

evaluation, we can eliminate ϕ since we are evaluating over one complete period of a periodic

function. Evaluation of this simplified function leads to Equations (21) and (22).

Appendix C: Evaluation of Fourier Coefficients in the Sphere-Plane Capacitor Model

Recall Equation (26) for the tip-sample capacitive force per unit mass

$$h_{s-p} = \frac{\omega^2 \pi \varepsilon'}{k} \cdot \frac{R^2}{\left(a \cdot Cos(\omega t + \phi) + p_o + l + \tau\right) \cdot \left(a \cdot Cos(\omega t + \phi) + p_o + l + \tau + R\right)} \quad (C1)$$

The zeroth order Fourier coefficient can be calculated by

$$h_o = \frac{\omega}{2\pi} \cdot \frac{\omega^2 \varepsilon' \pi R^2 V^2}{k} \int_{\frac{-\pi}{\omega}}^{\frac{\pi}{\omega}} \frac{1}{\left(a \cdot Cos(\omega t + \phi) + p_o + l + \tau\right) \cdot \left(a \cdot Cos(\omega t + \phi) + p_o + l + \tau + R\right)} dt \quad (C2)$$

which evaluates to Equation (27) when we assure that the tip never touches the substrate

$(a < po + l + \tau)$. Using the same trigonometric identities and methods as in Appendix B we can

evaluate h_{1r} and h_{1i}

$$h_{1r} = \frac{\omega}{\pi} \cdot \frac{\omega^2 \varepsilon' \pi R^2 V^2}{k} \int_{\frac{-\pi}{\omega}}^{\frac{\pi}{\omega}} \frac{Cos(\phi)Cos(\omega t + \phi)}{\left(a \cdot Cos(\omega t + \phi) + p_o + l + \tau\right) \cdot \left(a \cdot Cos(\omega t + \phi) + p_o + l + \tau + R\right)} dt$$

$$h_{1i} = \frac{\omega}{\pi} \cdot \frac{\omega^2 \varepsilon' \pi R^2 V^2}{k} \int_{\frac{-\pi}{\omega}}^{\frac{\pi}{\omega}} \frac{Sin(\phi)Cos(\omega t + \phi)}{\left(a \cdot Cos(\omega t + \phi) + p_o + l + \tau\right) \cdot \left(a \cdot Cos(\omega t + \phi) + p_o + l + \tau + R\right)} dt$$

since we can ignore all terms with the symmetric sine terms (see Appendix B). Equations (C3)

and (C4) evaluate to Equations (28) and (29) under the same restrictions as for the zeroth order

coefficient calculation above.

6. References

[1] G. Binning, C. Quate, and C. Gerber. *Phys. Rev. Lett.* **56,** 930 (1986).

[2] A. San Paulo and R. Garcia. *Biophys. J.* **78,** 1599 (2000).

[3] V Baranauskas, M Fontana, Zhao Jing Guo, H J Ceragioli A C Peterlevitz. *Nanotechnology.* **15,** 1661 (2004).

[4] Y G Kuznetsov, S Daijogo, J Zhou, B L Semler, and A McPherson. *Jour. Mol. Bio* .**347 (1),** 41 (2005).

[5] Y Wang, R Song, Y Li and J Shen. *Sur. Sci.* **530,** 136 (2003).

[6] F. Ohnesorge. *Surf. Interface Anal.* **27,** 379 (1999).

[7] A L Weisenhorn, M Egger, F Ohnesorge, S A C Gould, S P Heyn, H G Hansma, R L Sinsheimer, H E Gaub and P K Hansma. *Langmuir,* **7 (1),** 8 (1991).

[8] P K Hansma, J P Cleveland, M Radmacher, D A Walters, P E Hillner, M Bezanilla, M Fritz, D Vie, H G Hansma, C B Prater, J Massie, L Fukunaga, J Gurley, V Elings. *App. Phys. Lett.* **64 (13),** 1738 (1994).

[9] C D Frisbie, L F Rozsnyai, A Noy, M S Wrighton, C M Lieber. *Science* **265(5181),** 2071 (1994).

[10] A T Woolley, C Li, J H Hafner, C M Lieber. *Chem. And Bio.* **7,** 193 (2000).

[11] E.A. Boer, L.D. Bell, M. L. Brongersma, and H.A. Atwater. *Jour. App. Phys.* **90 (6),** 2764 (2001).

[12] Yu, A. A., Norville, J.E., Vaughn, M., Pacsial, E.J., Bruce, B.D., Baldo, M, Raymo, F, Stellacci, F. (unpublished manuscript).

[13] B Anczykowski, D Kruger, K L Babcock, H Fuchs. *Ultramicroscopy* **66,** 251 (1996).

[14] A Sebastian, M V Salapaka, D J Chen and J P Cleveland. *Jour App. Phys.* **89 (11),** 6473 (2001).

[15] A. Sebastian, M.V. Salapaka, D J Chen and J P Cleveland. Proceedings of the American Control Conference, San Diego, CA, (1999).

[16] M V Salapaka, D Chen, J P Cleveland. *Phys. Rev B.* **61,**1106 (2000).

[17] M V Salapaka, H S Berh, J Lai, A Majumdar, E McFarland. *J Appl. Phys.* **81,** 2480 (1997).

[18] Reproduced with permission of Prof. Christine Ortiz.

[19] Israelachvili, J. *Intermolecular and Surface Forces.* London: Academic Press, 1991.

[20] Smythe, W. R. *Static and Dynamic Electricity.* New York: McGraw-Hill, 1968.

[21] Oyama, Y., Majima, Y., Iwamoto, M. *Jour. App. Phys.* **86(12),** 7087 (1999).

[22] Hudlet, S, Saint Jean, M, Guthmann, C, Berger J. *Eur. Phys. J. B.* **2** 5(1998).

[23] Correspondence with Amy Yu (unpublished)